photonics

MDPI

Article

Design of an Achromatic Graphene Oxide Metalens with Multi-Wavelength for Visible Light

Yuxi Chen, Yongchang Ding, Haowen Yu and Xueyan Li *

Precision Measurement Laboratory, Zhejiang Sci-Tech University, Hangzhou 310018, China; 202120602082@mails.zstu.edu.cn (Y.C.); 202220701002@mails.zstu.edu.cn (Y.D.); 2023220705040@mails.zstu.edu.cn (H.Y.)
* Correspondence: xueyanli8023@zstu.edu.cn

Abstract: Dispersion control is a critical aspect in nano-optical systems. Moreover, chromatic aberration significantly impacts image quality. Despite metasurfaces being a novel approach to tackle chromatic aberration in diffractive lenses, numerous challenges hinder their practical implementation due to the complexity of 3D fabrication techniques and high manufacturing costs. In contrast, ultra-thin graphene oxide lenses are simpler and less expensive to manufacture. The optical performance of graphene oxide lenses, such as high focusing efficiency, large depth of field, wide bandwidth, and zooming capability, depends on the design of the positional arrangement of reduced graphene oxide regions. In this study, we utilized the self-constructed datasets to train machine learning models based on the structure of the graphene oxide lens and combined it with intelligent optimization algorithms. This approach facilitated the design of the graphene oxide achromatic lens in multi-wavelengths with high-performance. Experimental results substantiate that the designed ultra-thin graphene oxide lens, with a thickness of ~200 nm, effectively controls dispersion across multiple incident wavelengths (450, 550, and 650 nm) and achieves super resolution with consistent intensity at the focal point. Our graphene oxide lens holds the potential for integration into micro-optical systems that demand dispersion control, providing broad applications in optical imaging, optical communication, the biomedical field, and beyond.

Keywords: graphene oxide lens; multi-wavelength; achromatic focusing; machine learning

Citation: Chen, Y.; Ding, Y.; Yu, H.; Li, X. Design of an Achromatic Graphene Oxide Metalens with Multi-Wavelength for Visible Light. *Photonics* **2024**, *11*, 249. https://doi.org/10.3390/photonics11030249

Received: 1 February 2024
Revised: 6 March 2024
Accepted: 7 March 2024
Published: 11 March 2024

1. Introduction

Lenses in optical systems have diverse applications across multiple fields, including optical imaging [1,2], communication systems [3], biomedical research [4–7], and optical measurements [8]. Chromatic aberration is a phenomenon that occurs when light of different wavelengths converge at separate focal points upon passing through a lens which is caused by the dispersion effect and significantly impairs the imaging performance of optical systems [9]. Traditional methods of addressing the chromatic aberration is combining multiple lenses together [10] in achromatic lens designs, aimed at minimizing or eliminating this optical phenomenon. Nevertheless, the use of traditional lens combinations for achromatic effects is restricted due to the larger sizes and weights required, rendering them less suitable for applications in portable devices or nano-optical systems.

In recent years, the emergence of metasurfaces has introduced new opportunities for controlling dispersion in miniaturized optical systems. Basic principles of metasurface dispersion control involve changing the cross-sectional shape of the subwavelength structures [11–14], adjusting parameters of periodic structures [15–19], inverse design [20,21], or trying different combinations of regions [22,23]. As light passes through nanostructures, it refracts or reflects at varying angles, leading to diverse dispersion effects associated with different light frequencies. This dispersion control principle can also be applied to other optical devices for purposes like focusing, waveguiding, and dispersion compensation [24]. However, designing achromatic metasurfaces requires precise calculation of

the phase modulation of nanostructures, involving a computational-intensive process to create a library of nanostructures with varied characteristics and position them appropriately on the lens [25–27]. Meanwhile, to achieve optimal focusing performance with various wavelengths, the nanostructural units, acting as the fundamental component of the metasurface lens, are frequently composed of one or more substructures [28–30]. Nevertheless, the fabrication of such metalenses with multiple nanostructured units requires complex vacuum-assisted nanofabrication techniques, involving multiple steps such as patterning, etching, and cleaning [25]. Moreover, achieving high numerical-aperture (NA) focusing requires designing and constructing lenses with radii ranging from hundreds of micrometers to millimeters, as the size of each nanoelement in the metalens typically ranges from tens to hundreds of nanometers [18,21], significantly complicating the design and manufacturing process and imposing severe constraints on the range of applications for achromatic metasurfaces. Hence, the challenge remains to develop an achromatic ultra-thin planar lens that is computationally efficient, cost-effective, and structurally simple, while also being easy to manufacture.

Due to their superior optical properties, graphene and its derivatives, including graphene oxide (GO) and reduced graphene oxide (rGO), are increasingly being the preferred materials for ultra-thin flat lenses [31–34]. GO is derived from the oxidation process of graphene, which is a two-dimensional carbon material with a single-atomic thickness known for its remarkable optical properties, including high transparency and broad-spectrum absorption characteristics. rGO is obtained by the reduction of GO, resulting in a structure that closely resembles graphene, with decreased interlayer spacing. In contrast to GO, rGO exhibits significant changes in optical properties, such as an elevated refractive index and reduced transmittance, which is exactly used in modulating the electrical and optical properties of GO films by controlling the oxygen functional group content at various locations. Utilizing these properties to modulate the wavefront of GO, researchers have demonstrated a variety of GO lenses with applications in micro- and nano-optics [35,36], such as nanotracking [37].

Compared to the metalenses composed of nano-units, the fabrication of GO metalenses and the preparation of GO films are simpler [38]. GO metalenses can be fabricated in one-step using the direct laser-writing (DLW) [39] technique and can achieve high NA focusing while having a small size (a few micrometers) [36]. Furthermore, iterative optimization of the GO metalens structure using algorithms enables dispersion control with multiple wavelengths [40] and achieves super-resolution focusing. In this study, we present a GO metalens design capable of correcting color aberration with multiple wavelengths based on the Rayleigh–Sommerfeld (RS) diffraction theory. To achieve consistent focusing intensities at the various design wavelengths, we used RS diffraction theory and the Simulated Annealing (SA) algorithm [41] to establish the datasets which correlated the structural parameters, incident wavelengths, and focusing intensities of the GO metalens. Subsequently, we trained a Random Forest (RF) [42] model using the datasets, followed by employing the Genetic Algorithm (GA) [43] to optimize the model output and obtain the final lens structure. The experimental results reveal that the GO metalens we designed achieves super-resolution focusing, along with the ability to correct chromatic aberration at 450, 550, and 650 nm wavelengths, with the thickness of the GO metalens being ~200 nm.

2. Theoretical Model

2.1. Imaging Principle of Graphene Oxide Metalens

The schematic of the GO metalens focusing is shown in Figure 1a. The GO film adhered to a glass substrate (depicted by the blue region in Figure 1a) is processed into rGO regions (depicted by the yellow region in Figure 1a) using DLW technology. The optical properties of the processed regions, including transmission, refractive index, and thickness, undergo significant changes [36], as shown in Figure 1c, so that this structure of alternating rows of GO and rGO regions can modulate the incident wave. When an incident uniform plane wave $E_0(r_1, \theta_1)$ reaches the surface (r_1, θ_1) of the GO metalens, it

generates two different responses. A portion of the beams is absorbed and refracted by the rGO region, resulting in the modulation of both amplitude and phase, as shown in Figure 1c. The remaining beams propagating through the GO regions only experiences ignorable amplitude modulations. Consequently, the electric field modulated by the GO metalens can be expressed as follows:

$$E_1(r_1, \theta_1) = E_0(r_1, \theta_1) \cdot \sqrt{T(r_1, \theta_1)} \cdot e^{-ik\Delta\varphi(r_1, \theta_1)} \quad (1)$$

In Equation (1), $E_1(r_1, \theta_1)$ represents the electric field distribution resulting from the modulation of the amplitude and phase of the incident beam by the GO film. $T(r_1, \theta_1)$ denotes the distribution of transmission of the GO metalens, which can be calculated using the Beer–Lambert equation. $\Delta\varphi(r_1, \theta_1)$ is the phase modulation caused by the GO metalens consisting of GO regions and rGO regions.

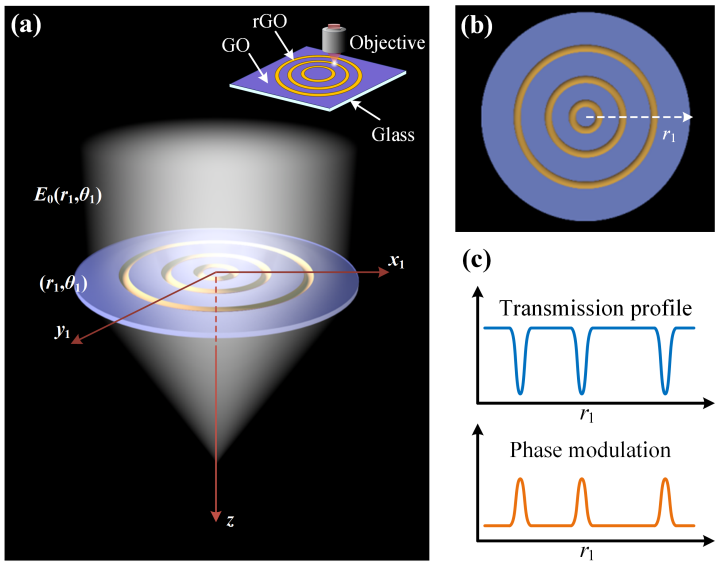

Figure 1. Schematic diagram of the focusing principle of a GO metalens. (**a**) The incident wave is modulated by the GO metalens, resulting in its convergence into a focal point. Distinct regions of the GO metalens are delineated using different colors, with the blue regions representing GO and the yellow regions representing rGO. (**b**) The GO and rGO regions of the GO metalens are arranged in an alternating pattern. (**c**) The transmission distribution and phase modulation of the GO lens along the direction indicated by arrow in (**b**).

After the process of lens fabrication, the alterations in refractive index $n(r_1, \theta_1)$, thickness $t(r_1, \theta_1)$, and extinction coefficient $K(r_1, \theta_1)$ due to the laser photoreduction can be formulated as follows:

$$\begin{cases} n(r_1, \theta_1) = n_{GO} + \Delta n \cdot M(r_1, \theta_1) \\ t(r_1, \theta_1) = t_{GO} + \Delta t \cdot M(r_1, \theta_1) \\ K(r_1, \theta_1) = K_{GO} + \Delta K \cdot M(r_1, \theta_1) \end{cases} \quad (2)$$

The modulation function M is defined as follows:

$$M(r_1, \theta_1) = C \sum_{m=1}^{N} e^{\frac{(r_1 - a_m)^2}{2w^2}} \quad (3)$$

Here, C is a constant determined by the power of the femtosecond laser. a_m is the central radius of the m^{th} rGO region, while N represents the total number of concentric circles containing rGO. According to the aforementioned GO metalens design method, the electric field distribution on the surface of the modulated lens can be accurately represented by determining the position of each rGO ring, and the electric field intensity at each point

in the optical field can be accurately calculated (Supplementary Materials, Section S1) by combining the RS diffraction theory [44].

2.2. Model of Multi-Wavelength Achromatic Aberration GO Metalens

The design of the multi-wavelength achromatic aberration GO metalens is based on modulating the incident light on the lens surface to achieve constructive interference at the focal point. Therefore, we need to establish an appropriate optimization model for the design requirements based on the RS diffraction principle to obtain a lens structure that can achieve achromatic super-resolution focusing for multiple discrete wavelengths. The focal point of the GO metalens is determined by the modulation of multiple GO and rGO regions. When there is light incident with a single wavelength, the GO metalens appropriately reshapes the wavefront through the alternating distribution of GO and rGO regions, enabling successful constructive interference of the transmitted light along the optical axis and ultimately focusing at the focal point. Furthermore, lenses with rGO regions of different widths and thicknesses demonstrate only slight variations in focusing performance, while significantly increasing the complexity and manufacturing cost. In this study, we adopt the same width and thickness for all rGO ring regions in the design process of the GO diffractive flat lens. Thus, the radius value is the sole parameter distinguishing each rGO region from others, describing the position information of each rGO region on the lens. It is crucial to determine the central radius of each rGO ring region as the impact on the field intensity at the focal point varies with various combinations of rGO region radii. Hence, our work uses the established model to find the optimal combination of rGO region radii for multi-wavelength achromatic focusing of the GO metalens.

To obtain a GO lens that meets design performance requirements, we need to optimize the parameters of the GO lens, i.e., the center radii $\mathbf{a}$ ($\mathbf{a} = [a_1, a_2, a_3, ..., a_m, ..., a_N]$, where a_m is the radius value of the mth rGO region) of the rGO regions. Prior to the optimization process, it becomes imperative to predefine the specifications and performance parameters governing the GO metalens (Supplementary Materials, Section S2).

Initially, we simulate and calculate the distribution of the modulated transmitted light, leveraging the principle of modulation of the optical field by the GO metalens. We establish the performance analysis model of the GO metalens, utilizing the RS diffraction principle, to calculate the intensity of the electric field at the focal point as follows:

$$E_2(f) = \int_0^\infty E_1(r_1)\left(-ik - \frac{1}{\sqrt{f^2 + {r_1}^2}}\right)\frac{\exp(-ik\sqrt{f^2 + {r_1}^2})}{f^2 + {r_1}^2} r_1 f dr_1 \quad (4)$$

where f is the focus length. $E_2(f)$ is the electric field distribution at the focus of the lens F, and $k = 2\pi/\lambda_i$ is the wavenumber. For the converging GO metalens, the upper limit of the integral in Equation (4) should be the radius of the GO lens, i.e., 200 μm. The light sources used for simulation and calculation are uniform plane waves with vertical incidence, with wavelengths denoted as λ_i, namely 450, 550, and 650 nm, respectively. The focal length is 100 μm to fit the design of a multi-wavelength chromatic aberration-correcting lens. Then, the SA algorithm was applied to optimize the intensity at the focal point of the GO lens in the RS diffraction model to build the dataset. The algorithmic mechanism of the SA algorithm is based on the iterative improvement of a single solution. At each iteration, the algorithm contemplates only the present solution alongside a randomly chosen adjacent solution and determines whether to adopt this novel solution according to the Metropolis criterion, thereby facilitating an escape from local optima in pursuit of the global optimum [45]. Due to its simple structure and speed [46,47], the SA algorithm was employed as the method for dataset generation in our study, particularly critical in scenarios demanding a reduction in the lens design cycle. The primary goal of the optimization process (main parameters of the algorithms can be found in Supplementary Materials, Section S3) is to maximize the light intensity $I = |E|^2$ at the focal point formed

by different incident wavelengths of the GO metalens to determine the model of the lens with dispersion control, which can be expressed as follows:

$$I(F, \lambda_i) = |E_2(\mathbf{a}, f, \lambda_i)|^2 \tag{5}$$

where $I(F, \lambda_i)$ is the intensity at the focus F of the GO metalens with the incident wavelength λ_i. $E_2(a, f, \lambda_i)$ indicates the electric field distribution at the focal point when the working wavelength is λ_i and the combination of rGO region radii is **a**. Additionally, in order for the lens design to focus at the focal point for all three incident wavelengths, the optimization criteria in this design are further modified to be

$$I(F) = \max\left\{ \sqrt[i]{\prod_i I(F, \lambda_i)} \right\} \tag{6}$$

In each iteration of generating and updating **a**, adjustments are made to each rGO region according to the constraints (Supplementary Materials, Section S2) to align with our simulation model. Various **a** and the corresponding optimization parameter $I(F)$ are generated during the optimization process. A crucial consideration is the potential for significant numerical differences among these focal intensities ($I(F, \lambda_i)$), which could result in diminished imaging performance.

To minimize the difference in intensity at the focus for various wavelengths, an independent study of the intensity of the focus formed by the three wavelengths was considered, as shown in Figure 2. The SA algorithm optimization objective $I(F)$ is calculated based on the focal intensity $I(F, \lambda_i)$ for three incident wavelengths. Therefore, we can easily record the three focal intensity values $I(F, \lambda_i)$ corresponding to different incident wavelengths for the same lens design **a** during the optimization process (note that **a** here changes randomly throughout the SA optimization process) and build three datasets **a**–$I(F, \lambda_1)$, **a**–$I(F, \lambda_2)$, and **a**–$I(F, \lambda_3)$ accordingly. For the purpose of ensuring that the light intensity at the focal point is as consistent as possible for different wavelengths of incidence for the final design of the lens, we divided the range of intensity values in the above three datasets into intervals and labeled the corresponding categories L_j in the order of the intervals to form three new datasets **a**–L_j–λ_1, **a**–L_j–λ_2, and **a**–L_j–λ_3 to train the RF model. RF, a potent machine learning algorithm, enhances prediction accuracy and robustness by combining multiple decision trees, each constructed using diverse subsets of data and features, thereby minimizing the risk of overfitting through random sampling and feature selection. Following that, under the same framework of the RF model, the training, validation, and testing sets from the three datasets are used to train three RF models, and the training time for each RF model at different wavelengths was less than 10 min.

After the completion of training for the three Random Forest Classification models (RFCMs), each classification model can be employed to determine the relationship between the set of $\mathbf{a} = [a_1, a_2, a_3, ..., a_m, ..., a_N]$ and the label (L_j) of the focal intensity value ($I(F, \lambda_i)$) in the case of incidence at the corresponding wavelengths. In contrast to the optimization method with modeling and numerical simulation for individual GO metalenses, this RF classification approach considerably alleviates the computational burden on computing resources. At the same time, this provides a viable way to reduce the difference in intensity at the focal point for different wavelengths. By inputting the identical combination of radius **a** into three RFCMs and employing specific selection methods, we can filter the model's outputs to identify the inputs and outputs that satisfy the given conditions. Through this optimization, the optimal combination of rGO region radii can be selected based on the three RFCMs, thereby fulfilling the requirements for chromatic aberration correction in the GO metalens.

The approach for selection is based on GA, which is a biologically inspired computational method that emulates the evolutionary processes observed in nature, enabling it to address optimization problems by simulating natural selection, genetic inheritance, and evolution. This evolutionary process of the GA can effectively leverage the diverse dataset

generated by the SA algorithm, demonstrating powerful global search capabilities when dealing with large-scale populations, which ensures superior quality of the optimization outcomes [47] and the lens designs. In the designed GO metalens described in this paper, each set of rGO region radii represents an individual, and the entire collection of different sets of region radii represents the population. Prior to the selection process, multiple initial combinations of 150 rGO region radii, meeting the constraints, are randomly generated to form multiple initial individuals, each consisting of 150 rGO region radii. Throughout the selection process, these combinations of rGO region radii undergo continuous changes.

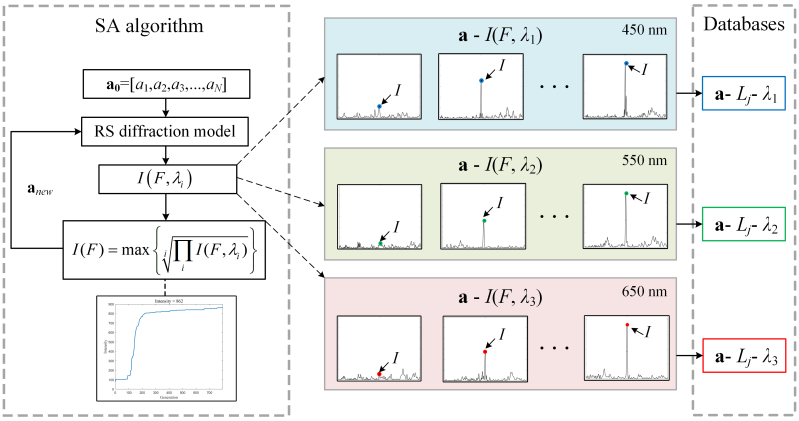

Figure 2. Schematic diagram of dataset construction. Applying RS diffraction theory, calculate the intensity at the focal point for different combinations of radii of rGO regions. The intensity values are categorized by wavelength and labeled based on their respective intensity intervals at the focal point. The distributions of the electric field intensity along the optical axis are simulated and calculated, and the distribution curves of the light intensity values along the optical axis are plotted. The intensity values are annotated using colors corresponding to wavelengths (blue, green, and red), and arrows are used for annotation.

In this study, we use the three trained RFCMs aforementioned to predict the labels L_{λ_i} that correspond to the electric field intensity at the focal point of the lens for various wavelength inputs (450, 550, and 650 nm), as shown in Figure 3. If the predicted labels from all three RFCMs are identical, we consider the lens designs to have consistent values of light intensity across different wavelengths. Therefore, the selection standard of GA is

$$\begin{cases} \max\{L_{\lambda_i}\} - \min\{L_{\lambda_i}\} = 0 \\ L_j = \max\{L_{\lambda_i}\} \end{cases} \tag{7}$$

By employing a sequence of competitive iterative procedures involving crossover and mutation, our objective is to ascertain the most adaptable population, which entails identifying the optimal combination of rGO ring radii that satisfy the specified selection criteria. Within Equation (6), a cohort manifesting the minimal discrepancy in electric field intensity at the focal point, across different wavelengths, is chosen, favoring a heightened focal intensity value. The natural selection simulation is conducted over 50 iterations, requiring approximately 600 s.

To summarize, the SA optimization algorithm is used to construct $\mathbf{a}$–L_j–λ_i datasets associated with different design wavelengths λ_i. These datasets are leveraged to train RFCMs tailored for three distinct design wavelengths. This training equips RFCMs with the capability to forecast the numerical interval of the intensity at the focal point resulting from transmitted light modulation by the lens. Subsequently, GA are applied to select the anticipated outputs of the three trained RFCMs as targets, with the goal of discerning the input parameters that correspond to optimal outputs. This iterative process is designed to ascertain the combination of rGO ring radii that facilitates the attainment of optimal chromatic aberration correction performance by the GO metalens.

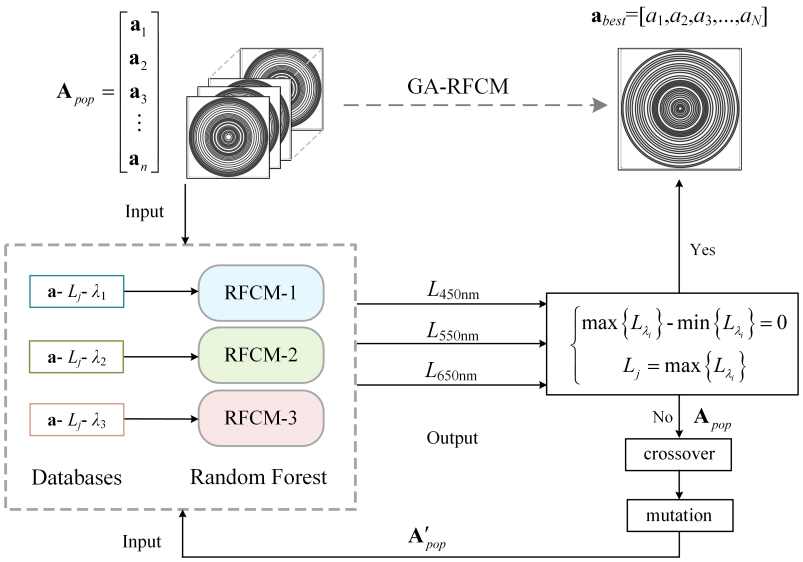

Figure 3. Optimization and selection process of GO lens design. The output of the RFCM (the labels of the light intensity interval at the focal point) is optimized using the GA and select input features (the radii of the rGO regions) based on the optimization criteria.

3. Results and Discussion

3.1. Optimized Design of Achromatic Graphene Oxide Metalens

We first design the optimal combination of radius values for arranging multiple rGO rings on a GO substrate to correct the chromatic aberration by GA selection. The cumulative time required for designing the GO metalens is less than 185 h, consisting of 184 h for dataset construction (15,000 data points), 10 min for RFCM training, and 10 min for selecting the optimal combination of rGO rings (150 rGO rings). In contrast, when employing the same computational hardware to design the GO metalens, by depending solely on a simulation model built based on the imaging principle of the GO metalens for performing numerical simulations and iterative optimizations, the process may require a minimum of 250 h. The design approach based on RFCMs significantly reduces the time required during the optimization selection process, allowing for greater flexibility in adjustments.

According to the design of the GO metalens, the minimum radius a_1 for the rGO rings is 1.45 μm, and the maximum radius a_{150} is 199.843 μm, as shown in Figure 4a. The specific radii for the remaining rings can be found in the Supplementary Materials, Section S4. Each ring has a linewidth of 0.8 μm, and the center-to-center distance (d) between adjacent rings is at least 0.9 μm, ensuring an alternating distribution between the GO and rGO regions. Then, we utilized the established GO metalens performance analysis model to simulate and calculate the modulation of incident light with the wavelength of 450, 550, and 650 nm, aiming to evaluate the modulation characteristics of the optimized GO lens design on the incident light. As shown in Figure 5, the plane wave can be theoretically modulated by the lens to exhibit a significant distribution of electric field intensity near the predetermined focal point, which means that the GO metalens design predicted by RFCM is consistent with the mathematical model. It is noteworthy that the intensities of the focal points formed by three wavelengths are nearly identical, thanks to the interval partitioning of light intensity during the design of the GO lens.

To validate the accuracy of the optimized design, the GO lens was fabricated using direct laser writing with a femtosecond laser (800 nm, 100 fs, 10 kHz, the preparation of the GO film sample and the fabrication of the GO metalens can be found in Supplementary Materials, Section S5). Figure 4c displays the microscopic image of the GO metalens, with the dark regions indicating the areas of rGO (details can be found in the Supplementary Materials, Section S6). The thickness of the GO region is ~200 nm, while

the thickness of the rGO region is ~100 nm. The effect of variations in laser processing linewidth, processing thickness, and contour distribution on the chromatic aberration imaging quality of the GO metalens is minimal.

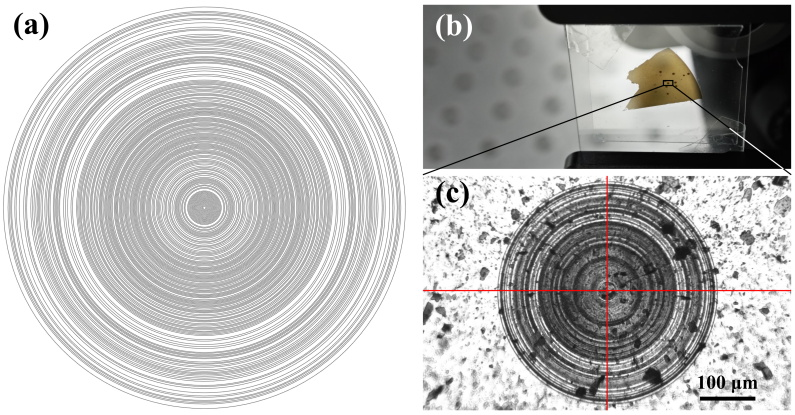

Figure 4. The design of chromatic GO metalens. (**a**) The two-dimensional layout of GO metalens. (**b**) GO film on slide. (**c**) Microscope image of the fabricated GO lens. Scale bar: 100 μm.

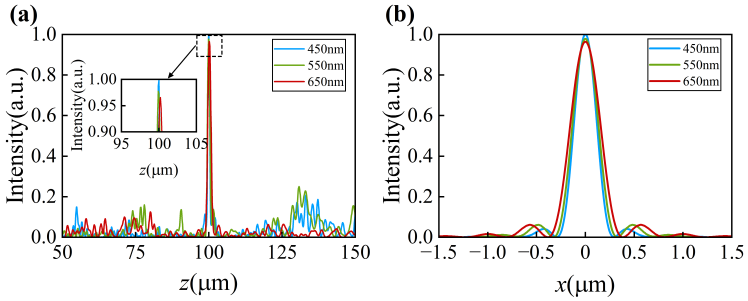

Figure 5. Intensity distribution curve near the focal point calculated based on the GO lens model. (**a**) Theoretical curves of intensity distribution along the optical axis at wavelengths of 450, 550, and 650nm. (**b**) Theoretical curve of radial intensity distribution at the focal point.

3.2. Achromatic Focusing Characterization

The focal intensity distribution of the GO achromatic lens is measured using a microscope characterization setup (Supplementary Materials, Section S7). Incident light from lasers with wavelengths of 450, 550, and 650 nm are expanded into approximate plane waves before being focused by the GO metalens. The experimentally measured focal intensity profiles of the optical axis plane (x–z) and the radial plane (x–y) and corresponding theoretical results with wavelengths (450, 550, and 650 nm) are shown in Figure 6, respectively.

Figure 6 depicts the distribution of the electric field in both the axial plane and focal plane for various incident wavelengths, including data obtained from simulation calculations and experimental measurements conducted. A strong consistency can be observed between the results of experimental measurements and theoretical simulations. The axial distribution of focal points exhibits slight tilting and minor asymmetry in the vertical direction, possibly attributed to the unevenness of the light source emitted by the laser. To further demonstrate the agreement between the measured results and theoretical calculations, we plotted the intensity of the electric field along the dashed line in Figure 6e,f, as depicted in Figure 6g,h. In Figure 6g, with an incident wavelength of 650 nm, the light intensity distribution curve near the focal point at an incident wavelength of 650 nm matches the theoretical distribution curve, and the focal length of the GO lens has theoretical and measured values of 100.2 μm and 100.4 μm, respectively. Moreover, Figure 6h shows that the radial distribution of the intensity of the focal spot in the focal plane exhibits excellent symmetry, thus further demonstrating the reliability of the RS diffraction theory in simulating the GO lens.

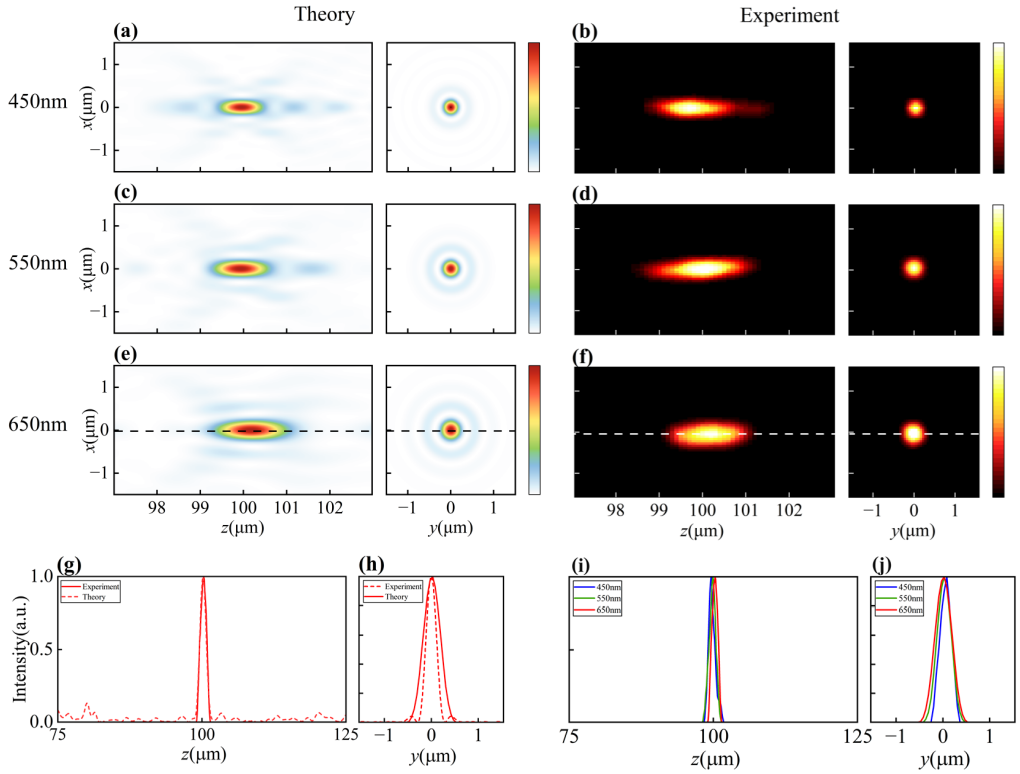

Figure 6. Comparison of experimental and theoretical GO lens achromatic properties. (**a**,**c**,**e**) Theoretical intensity distribution in the axial and radial planes near the focal point of the GO lens with three wavelengths of 450, 550, and 650 nm. (**b**,**d**,**f**) Experimental intensity distribution in the axial and radial planes near the focal point of the GO lens with three wavelengths of 450, 550, and 650 nm. (**g**,**h**) Intensity distribution curves along the dashed lines in (**e**,**f**). (**i**,**j**) Experimentally measured focal intensity distributions along axial and radial directions with wavelengths of 450, 550, and 650 nm.

To observe the impact of various wavelengths on the focal length of the GO lens, the focal length was measured at three working wavelengths, and the results are shown in Figure 7a. The results indicate that the focal lengths of the lens when illuminated with three wavelengths are all approximately 100 μm, with an average focal length $\bar{f}$ ($\bar{f} = \frac{1}{n}\sum_{k=1}^{n} f_k$, where f_k is the focal length corresponding to each wavelength) of 99.93 μm. The average deviation ($\frac{1}{n}\sum_{k=1}^{n} |f_k - f_d|$, where f_d is the theoretical focal length during lens design) between the actual focal length corresponding to each wavelength and the theoretical focal length is 0.167 μm. The focal lengths in the experimental results exhibit good consistency. The slight difference between the actual and theoretical focal lengths is mainly due to the need for processing numerous and dense rGO regions on the surface of the designed GO metalens, which results in inconsistencies in the morphology between the rGO regions during lens fabrication. Additionally, in the characterization experiment of the GO metalens, errors generated during the movement of the piezoelectric displacement stage can also have a slight impact on the actual focal length. Based on the focal length, the numerical aperture (NA) of the GO metalens is approximately 0.894.

Based on the measured normalized intensity profiles in the radial direction of the focal point in Figure 6j, it is possible to obtain the full width at half maximum (FWHM) of the focal spot at different wavelengths to verify the super-resolution capability of the GO metalens that was designed. In the focal plane, the measured FWHM_{radial} for the actual focal points, when the incidence wavelengths are 450, 550, and 650 nm, are 0.280 μm (0.624 λ), 0.311 μm (0.565 λ), and 0.386 μm (0.594 λ), respectively, as shown in Figure 7b. The differences

between the experimental results and the theoretical values of the FWHM are 9.8%, 6.4%, and 11.8%, respectively. Nevertheless, it is worthy to note that, according to the Rayleigh criterion ($\frac{0.61\lambda}{NA}$), the incident light of different wavelengths modulated by GO metalens can still form focal spots with the super-resolution capability on the focal plane. The aforementioned experimental results demonstrate that by employing design parameters with a high numerical aperture (NA = 0.894), the focal point of the GO metalens design can exceed the diffraction limit for each wavelength, enabling sub-wavelength resolution imaging. This attribute is of paramount importance for applications that demand high-quality images, particularly in fields like microscopy and optical instrument manufacturing.

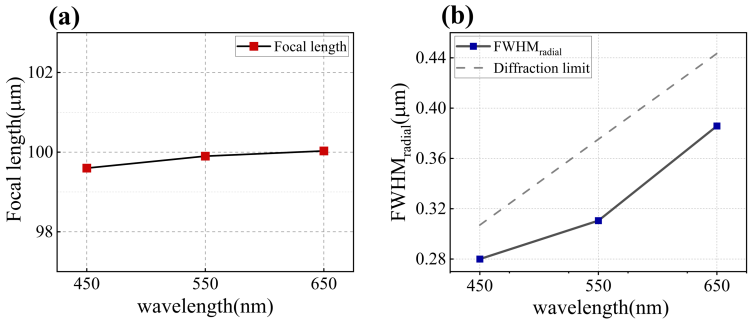

Figure 7. Focal lengths and FWHM$_{radial}$ of the focal points as the functions of the wavelength. (**a**) The focal lengths of the GO lens measured at incident light wavelengths of 450, 550, and 650 nm. (**b**) Radial FWHM of the focal points and the diffraction limit.

4. Conclusions

In summary, based on RS diffraction theory, we combined machine learning and intelligent optimization algorithms to present a chromatic aberration-correcting GO lens design capable of dispersion control across multiple wavelengths, with a thickness of 200 μm. Both theoretically and experimentally, we showcased a chromatic aberration-correcting performance in the GO metalens, maintaining a consistent focal length when illuminated at wavelengths of 450, 550, and 650 nm. By employing a high numerical aperture design, the radial FWHM of the GO lens's focal spots exceed the diffraction limit. This achievement holds significant implications for the miniaturization of optical instruments requiring high resolution, such as smartphone cameras, super-resolution microscopes, and endoscopes. Furthermore, compared to metasurface lenses (both the metallic and dielectric ones), our chromatic aberration-correcting GO lens offers the advantage of further thickness reduction. Additionally, the GO lens fabrication through DLW technology facilitates its industrial production, crucial for the manufacturing of miniaturized flat lenses.

Supplementary Materials: The following supporting information can be downloaded at: https://www.mdpi.com/article/10.3390/photonics11030249/s1, Figure S1: Theoretical model schematic of GO metalens; Figure S2: Imaging model of the GO lens based on the RS diffraction theory; Figure S3: Direct laser fabrication system; Figure S4: Localized magnification of the GO lens; Figure S5: Experiment setup of optical characterization; Table S1: Main preset parameters of graphene oxide metalens; Table S2: The main parameters of the SA algorithm; Table S3: The main parameters of the GA; Table S4: The principal parameters of the random forest; Table S5: Design of the Graphene Metalens.

Author Contributions: Investigation, Y.C., Y.D. and H.Y.; Methodology, Y.C.; Project administration, X.L.; Resources, X.L.; Software, Y.C.; Supervision, X.L.; Visualization, Y.C., Y.D. and H.Y.; Writing—original draft, Y.C.; Writing—review and editing, X.L. All authors have read and agreed to the published version of the manuscript.

Funding: This research was supported by the Zhejiang Provincial Natural Science Foundation of China under Grant No. LQ23F050014. This research was supported by the Scientific Research Foundation of Zhejiang Sci-Tech University under Grand No. 21022248-Y.

Institutional Review Board Statement: Not applicable.

Informed Consent Statement: Not applicable.

Data Availability Statement: Data are contained within the article and the Supplementary Materials.

Conflicts of Interest: The authors declare no conflicts of interest.

References

1. Zhu, W.; Duan, F.; Tatsumi, K.; Beaucamp, A. Monolithic topological honeycomb lens for achromatic focusing and imaging. *Optica* **2022**, *9*, 100–107. [CrossRef]
2. Pinilla, S.; Rostami, S.R.M.; Shevkunov, I.; Katkovnik, V.; Egiazarian, K. Hybrid diffractive optics design via hardware-in-the-loop methodology for achromatic extended-depth-of-field imaging. *Opt. Express* **2022**, *30*, 32633–32649. [CrossRef] [PubMed]
3. Liu, Z.; Yang, L.; Yang, Y.; Wu, R.; Zhang, L.; Chen, L.; Wu, D.; She, J. Improved optical camera communication systems using a freeform lens. *Opt. Express* **2021**, *29*, 34066–34076. [CrossRef] [PubMed]
4. Dholakia, K.; Drinkwater, B.W.; Ritsch-Marte, M. Comparing acoustic and optical forces for biomedical research. *Nat. Rev. Phys.* **2020**, *2*, 480–491. [CrossRef]
5. Luo, Y.; Chu, C.H.; Vyas, S.; Kuo, H.Y.; Chia, Y.H.; Chen, M.K.; Shi, X.; Tanaka, T.; Misawa, H.; Huang, Y.Y.; et al. Varifocal metalens for optical sectioning fluorescence microscopy. *Nano Lett.* **2021**, *21*, 5133–5142. [CrossRef] [PubMed]
6. Coste, A.; Oktay, M.H.; Condeelis, J.S.; Entenberg, D. Intravital imaging techniques for biomedical and clinical research. *Cytom. Part A* **2020**, *97*, 448–457. [CrossRef] [PubMed]
7. Huang, Z.; Zheng, Y.; Li, J.; Cheng, Y.; Wang, J.; Zhou, Z.K.; Chen, L. High-resolution metalens imaging polarimetry. *Nano Lett.* **2023**, *23*, 10991–10997. [CrossRef] [PubMed]
8. Bai, J.; Li, X.; Wang, X.; Wang, J.; Ni, K.; Zhou, Q. Self-reference dispersion correction for chromatic confocal displacement measurement. *Opt. Lasers Eng.* **2021**, *140*, 106540. [CrossRef]
9. Hecht, E. *Optics*; Pearson Education India: Delhi, India, 2012.
10. Sun, W.S.; Tien, C.L.; Liang, S.S.; Lin, J.S. A Cost-Effective Triplet Lens Design with Chromatic Aberration Correction Based on Optimization Algorithm and Illustration Method. *Appl. Sci.* **2022**, *12*, 11881. [CrossRef]
11. Shrestha, S.; Overvig, A.C.; Lu, M.; Stein, A.; Yu, N. Broadband achromatic dielectric metalenses. *Light Sci. Appl.* **2018**, *7*, 85. [CrossRef]
12. Ndao, A.; Hsu, L.; Ha, J.; Park, J.H.; Chang-Hasnain, C.; Kanté, B. Octave bandwidth photonic fishnet-achromatic-metalens. *Nat. Commun.* **2020**, *11*, 3205. [CrossRef] [PubMed]
13. Chen, M.K.; Wu, Y.; Feng, L.; Fan, Q.; Lu, M.; Xu, T.; Tsai, D.P. Principles, functions, and applications of optical meta-lens. *Adv. Opt. Mater.* **2021**, *9*, 2001414. [CrossRef]
14. Zhang, L.; Wang, C.; Wei, Y.; Lin, Y.; Han, Y.; Deng, Y. High-Efficiency Achromatic Metalens Topologically Optimized in the Visible. *Nanomaterials* **2023**, *13*, 890. [CrossRef] [PubMed]
15. Dou, K.; Xie, X.; Pu, M.; Li, X.; Ma, X.; Wang, C.; Luo, X. Off-axis multi-wavelength dispersion controlling metalens for multi-color imaging. *Opto-Electron. Adv.* **2020**, *3*, 190005-1. [CrossRef]
16. Khorasaninejad, M.; Shi, Z.; Zhu, A.Y.; Chen, W.T.; Sanjeev, V.; Zaidi, A.; Capasso, F. Achromatic metalens over 60 nm bandwidth in the visible and metalens with reverse chromatic dispersion. *Nano Lett.* **2017**, *17*, 1819–1824. [CrossRef] [PubMed]
17. Aiello, M.D.; Backer, A.S.; Sapon, A.J.; Smits, J.; Perreault, J.D.; Llull, P.; Acosta, V.M. Achromatic varifocal metalens for the visible spectrum. *ACS Photonics* **2019**, *6*, 2432–2440. [CrossRef]
18. Baek, S.; Kim, J.; Kim, Y.; Cho, W.S.; Badloe, T.; Moon, S.W.; Rho, J.; Lee, J.L. High numerical aperture RGB achromatic metalens in the visible. *Photonics Res.* **2022**, *10*, B30–B39. [CrossRef]
19. Qian, Z.; Tian, S.; Zhou, W.; Wang, J.; Guo, H. Broadband achromatic longitudinal bifocal metalens in the visible range based on a single nanofin unit cell. *Opt. Express* **2022**, *30*, 11203–11216. [CrossRef]
20. Chung, H.; Miller, O.D. High-NA achromatic metalenses by inverse design. *Opt. Express* **2020**, *28*, 6945–6965. [CrossRef]
21. Li, Z.; Pestourie, R.; Park, J.S.; Huang, Y.W.; Johnson, S.G.; Capasso, F. Inverse design enables large-scale high-performance meta-optics reshaping virtual reality. *Nat. Commun.* **2022**, *13*, 2409. [CrossRef]
22. Shen, S.; Li, S.; Yuan, Y.; Tan, H. High-efficiency broadband achromatic metalenses for visible full-stokes polarization imaging. *Opt. Express* **2023**, *31*, 28611–28623. [CrossRef]
23. Huang, L.; Colburn, S.; Zhan, A.; Majumdar, A. Full-Color Metaoptical Imaging in Visible Light. *Adv. Photonics Res.* **2022**, *3*, 2100265. [CrossRef]
24. Pan, M.; Fu, Y.; Zheng, M.; Chen, H.; Zang, Y.; Duan, H.; Li, Q.; Qiu, M.; Hu, Y. Dielectric metalens for miniaturized imaging systems: Progress and challenges. *Light Sci. Appl.* **2022**, *11*, 195. [CrossRef] [PubMed]
25. Fan, Z.B.; Qiu, H.Y.; Zhang, H.L.; Pang, X.N.; Zhou, L.D.; Liu, L.; Ren, H.; Wang, Q.H.; Dong, J.W. A broadband achromatic metalens array for integral imaging in the visible. *Light Sci. Appl.* **2019**, *8*, 67. [CrossRef] [PubMed]
26. Elsawy, M.M.; Gourdin, A.; Binois, M.; Duvigneau, R.; Felbacq, D.; Khadir, S.; Genevet, P.; Lanteri, S. Multiobjective statistical learning optimization of RGB metalens. *ACS Photonics* **2021**, *8*, 2498–2508. [CrossRef]
27. Wang, F.; Geng, G.; Wang, X.; Li, J.; Bai, Y.; Li, J.; Wen, Y.; Li, B.; Sun, J.; Zhou, J. Visible achromatic metalens design based on artificial neural network. *Adv. Opt. Mater.* **2022**, *10*, 2101842. [CrossRef]

28. Chen, W.T.; Zhu, A.Y.; Sanjeev, V.; Khorasaninejad, M.; Shi, Z.; Lee, E.; Capasso, F. A broadband achromatic metalens for focusing and imaging in the visible. *Nat. Nanotechnol.* **2018**, *13*, 220–226. [CrossRef] [PubMed]
29. Chen, W.T.; Zhu, A.Y.; Sisler, J.; Bharwani, Z.; Capasso, F. A broadband achromatic polarization-insensitive metalens consisting of anisotropic nanostructures. *Nat. Commun.* **2019**, *10*, 355. [CrossRef]
30. Dai, X.; Dong, F.; Zhang, K.; Liao, D.; Li, S.; Shang, Z.; Zhou, Y.; Liang, G.; Zhang, Z.; Wen, Z.; et al. Holographic super-resolution metalens for achromatic sub-wavelength focusing. *ACS Photonics* **2021**, *8*, 2294–2303. [CrossRef]
31. Koppens, F.; Mueller, T.; Avouris, P.; Ferrari, A.; Vitiello, M.; Polini, M. Photodetectors based on graphene, other two-dimensional materials and hybrid systems. *Nat. Nanotechnol.* **2014**, *9*, 780–793. [CrossRef]
32. Cao, G.; Lin, H.; Fraser, S.; Zheng, X.; Del Rosal, B.; Gan, Z.; Wei, S.; Gan, X.; Jia, B. Resilient graphene ultrathin flat lens in aerospace, chemical, and biological harsh environments. *ACS Appl. Mater. Interfaces* **2019**, *11*, 20298–20303. [CrossRef]
33. Lin, H.; Sturmberg, B.C.; Lin, K.T.; Yang, Y.; Zheng, X.; Chong, T.K.; de Sterke, C.M.; Jia, B. A 90-nm-thick graphene metamaterial for strong and extremely broadband absorption of unpolarized light. *Nat. Photonics* **2019**, *13*, 270–276. [CrossRef]
34. Yang, D.; Cheng, Y.; Chen, F.; Luo, H.; Wu, L. Efficiency tunable broadband terahertz graphene metasurface for circular polarization anomalous reflection and plane focusing effect. *Diam. Relat. Mater.* **2023**, *131*, 109605. [CrossRef]
35. Wei, S.; Cao, G.; Lin, H.; Yuan, X.; Somekh, M.; Jia, B. A varifocal graphene metalens for broadband zoom imaging covering the entire visible region. *ACS Nano* **2021**, *15*, 4769–4776. [CrossRef] [PubMed]
36. Zheng, X.; Jia, B.; Lin, H.; Qiu, L.; Li, D.; Gu, M. Highly efficient and ultra-broadband graphene oxide ultrathin lenses with three-dimensional subwavelength focusing. *Nat. Commun.* **2015**, *6*, 8433. [CrossRef] [PubMed]
37. Li, X.; Wei, S.; Cao, G.; Lin, H.; Zhao, Y.; Jia, B. Graphene metalens for particle nanotracking. *Photonics Res.* **2020**, *8*, 1316–1322. [CrossRef]
38. Zhang, S.; Li, Y.; Pan, N. Graphene based supercapacitor fabricated by vacuum filtration deposition. *J. Power Sources* **2012**, *206*, 476–482. [CrossRef]
39. Wang, S.; Zhou, Z.; Li, B.; Wang, C.; Liu, Q. Progresses on new generation laser direct writing technique. *Mater. Today Nano* **2021**, *16*, 100142. [CrossRef]
40. Li, X.; Meng, F.; Chen, Y.; Xu, Y. Designer graphene oxide ultrathin flat lens with versatile focusing property. *Opt. Express* **2024**, *32*, 6531–6539. [CrossRef]
41. Aarts, E.; Korst, J.; Michiels, W. Simulated annealing. In *Search Methodologies: Introductory Tutorials in Optimization and Decision Support Techniques*; Springer: New York, NY, USA, 2005; pp. 187–210.
42. Biau, G.; Scornet, E. A random forest guided tour. *Test* **2016**, *25*, 197–227. [CrossRef]
43. Lambora, A.; Gupta, K.; Chopra, K. Genetic algorithm—A literature review. In Proceedings of the 2019 International Conference on Machine Learning, Big Data, Cloud and Parallel Computing (COMITCon), Faridabad, India, 14–16 February 2019; IEEE: San Francisco, CA, USA, 2019; pp. 380–384.
44. Cao, G.; Gan, X.; Lin, H.; Jia, B. An accurate design of graphene oxide ultrathin flat lens based on Rayleigh-Sommerfeld theory. *Opto-Electron. Adv.* **2018**, *1*, 180012-1. [CrossRef]
45. Delahaye, D.; Chaimatanan, S.; Mongeau, M. Simulated annealing: From basics to applications. In *Handbook of Metaheuristics*; Springer: Cham, Switzerland, 2019; pp. 1–35.
46. Çetin, G.; Keçebaş, A. Optimization of thermodynamic performance with simulated annealing algorithm: A geothermal power plant. *Renew. Energy* **2021**, *172*, 968–982. [CrossRef]
47. Otubamowo, K.; Egunjobi, T.; Adewole, A. A comparative study of simulated annealing and genetic algorithm for solving the travelling salesman problem. *Int. J. Appl. Inf. Syst.* **2012**, *4*, 6–12.